

# Transient Adsorption Behavior of Single Fluorophores on an Electrode-Supported Nanobubble

Wes R. Leininger, Zhuoyu Peng, and Bo Zhang\*



Cite This: *Chem. Biomed. Imaging* 2023, 1, 380–386



Read Online

ACCESS |



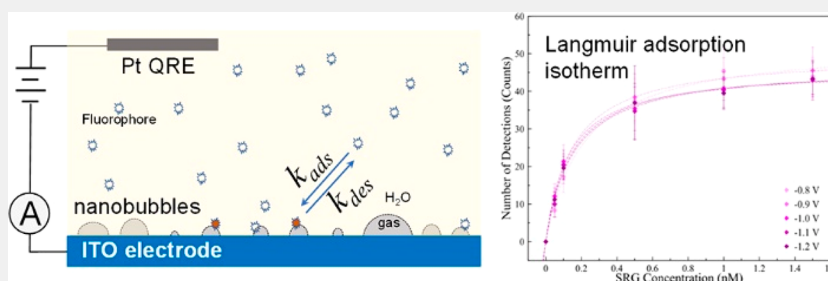
Metrics & More



Article Recommendations



Supporting Information



**ABSTRACT:** Here we report the use of a Langmuir isotherm model to analyze and better understand the dynamic adsorption and desorption behavior of single fluorophore molecules at the surface of a hydrogen nanobubble supported on an indium tin oxide (ITO) electrode. Three rhodamine dyes, rhodamine 110 (R110, positively charged), rhodamine 6G (R6G, positively charged), and sulforhodamine G (SRG, negatively charged) were chosen for this study. The use of the Langmuir isotherm model allows us to determine the equilibrium constant and the rate constants for the adsorption and desorption processes. Of the three fluorophores used in this study, SRG was found to have the greatest equilibrium constant. No significant potential dependence was observed on the adsorption characteristics, which suggests the nanobubble size, geometry, and surface properties are relatively constant within the range of potentials used in this study. Our results suggest that the use of the Langmuir isotherm model is a valid and useful means for probing and better understanding the unique adsorption behavior of fluorophores at surface-supported nanobubbles.

**KEYWORDS:** *Electrochemical, Langmuir isotherm, nanobubble, adsorption kinetics, fluorophore, chemical interface*

## INTRODUCTION

The chemical interface is a unique region in chemical systems with properties and phenomena that differ from the bulk. Many studies have been pursued across various fields, including biological membranes,<sup>1</sup> air/ocean interfaces,<sup>2</sup> atmospheric chemistry,<sup>3,4</sup> catalysis,<sup>5</sup> and numerous electrochemical applications<sup>6–9</sup> among others.<sup>10</sup> Aqueous interfaces, such as air/water or electrode/solution systems, are of particular interest as they lend understanding to fundamental events such as the Hofmeister series, which characterizes protein stability in ionic solutions;<sup>11</sup> amphoteric organic molecules at ocean surfaces;<sup>12</sup> and catalytic activity, corrosion, and electrolysis at the solution/electrode interface.<sup>13–15</sup>

Analytical techniques used to study the chemical interface are somewhat limited due to the interface being an ultrathin region; therefore, any instrument used must be able to probe down to the molecular level. Commonly used analysis methods include photoelectron spectroscopy,<sup>16</sup> neutron reflectivity,<sup>17</sup> and vibrational sum-frequency generation with infrared wavelength.<sup>18–22</sup> The Saykally group used resonant UV second harmonic generation spectroscopy combined with computational work to study the adsorption mechanism of thiocyanate ions at the air/water interface.<sup>23–25</sup> The Richmond group

utilized vibrational sum frequency spectroscopy to study different small organic molecules at the air/water interface to reveal molecular level information related to atmospheric aerosols.<sup>4,26</sup> Despite their ability to probe the interface, nonlinear optical techniques mainly measure the average ensemble behavior of molecules at the interface. On the other hand, single-molecule fluorescence microscopy has been developed and used to probe interfacial behavior of single molecules.<sup>27</sup>

Using these single-entity detection methods, Harris and co-workers studied interfacial DNA hybridization kinetics at selective capture surfaces<sup>28,29</sup> and measured the binding rates of proteins at a phospholipid bilayer via fluorescence microscopy.<sup>30</sup> A previous study published by our group utilized total internal reflection fluorescence (TIRF) microscopy to study single redox events at a modified indium tin

**Received:** February 1, 2023

**Revised:** March 8, 2023

**Accepted:** March 13, 2023

**Published:** March 23, 2023



oxide (ITO) surface, where the adsorption, desorption, and redox dynamics were studied in detail.<sup>7</sup> Later, we successfully imaged the electrochemically generated surface nanobubbles via single fluorophore labeling.<sup>6</sup> This approach creates a unique nanoscale gas/liquid/solid three-phase boundary allowing one to study different interfaces simultaneously.

To better understand molecular adsorption at nanobubble surfaces and to reveal the detailed mechanistic properties, the Langmuir isotherm adsorption model<sup>31</sup> can be applied to elucidate the interfacial adsorption behavior of rhodamine fluorophores on the surface of electrode supported H<sub>2</sub> nanobubbles. Typically used to describe the adsorption of gas onto a solid surface,<sup>32</sup> the Langmuir isotherm model can be modified to fit this system by expressing the surface coverage as a function of the concentration of the adsorbing dye. The use of this model provides a direct way to determine the equilibrium constant of adsorption, which in turn will be used to decipher the interactions of the dyes at the nanobubble surface. Each nanobubble is a distinct nanoscale gas/liquid interface that we can use to resolve individual fluorophores' adsorption and provide direct mechanistic insights to the kinetics of adsorption and desorption. Three rhodamine dyes with different charges, rhodamine 110 (R110) and rhodamine 6G (R6G), both positively charged, and the negatively charged sulforhodamine G (SRG), were chosen. SRG was observed to have the greatest equilibrium constant—possibly due to a preferred molecular orientation at the bubble surface.

## EXPERIMENTAL SECTION

### Chemicals and Materials

All of the following chemicals and materials were used as received from the manufacturers: rhodamine 6G perchlorate (R6G; Kodak, laser grade), sulforhodamine G (SRG; Aldrich Chemical Co.; fluorophore content ~60%), rhodamine 110 (R110; Lambda Physik), sodium sulfate (Na<sub>2</sub>SO<sub>4</sub>; J. T. Baker, 101.8%), and ITO-coated microscope coverslips (SPI Supplies, sheet resistance 15–30 Ω/square). Deionized water (>18 MΩ·cm) was obtained through a Barnstead Nanopure water purification system and used for all aqueous solutions.

### Single-Molecule TIRF Microscopy

Single-molecule imaging experiments were performed on a home-built TIRF system based on an Olympus IX70 inverted microscope. An Olympus Apo N 60× 1.49 NA objective (with an external 1.5× magnification on the microscope) and a 532 nm green laser (CrystaLaser) source were used. With a constant 10 mW (2.5 kW/cm<sup>2</sup>) excitation illumination, the fluorescence images were filtered with an ET590/50m emission filter (Chroma Technology Co.) and collected on an EMCCD (iXon Ultra 897, Andor) cooled to −85 °C. Images were recorded at 0.05 s exposure time (frame rate 19.81 Hz) and with an amplifier gain of 300. A thin polydimethylsiloxane (PDMS) film with a 2 mm diameter hole was placed on the surface of the ITO electrode. 6 μL of dye solution was placed in the hole and a piece of Pt wire (0.5 mm diameter) was placed in the solution as a quasi-reference electrode (QRE). The voltage was generated by a Pine AFCBP1 potentiostat (Pine Instrument) and applied across the working electrode (ITO) with respect to the Pt QRE.

### Image Analysis and Counting Single Molecules

Single-molecule fluorescence images and videos were analyzed using the ThunderSTORM plug-in in ImageJ.<sup>33</sup> Each fluorescent single-molecular spot is described by a point spread function (PSF), which is fitted with a two-dimensional (2-D) Gaussian function to localize the center position. A total number of fluorescent spots were counted as the number of detections. The number of detections was plotted as a function of the fluorophore concentration. The Langmuir equation

(eq 2) was used to fit the data points, and the equilibrium constants were determined.

### Single-Molecule Tracking

Tracking of fluorescent puncta was performed using the TrackMate plug-in in ImageJ.<sup>34</sup> Briefly, fluorescent puncta were detected above a user-set threshold using the Laplacian of the Gaussian (LoG) as a blob detector. Puncta were tracked and linked to other puncta within three frames within 300 nm displacement. The number of frames for one trajectory was converted to duration times using a frame rate of 19.81 Hz.

## RESULTS AND DISCUSSION

All experimental conditions were similar to what was previously used in nanobubble generation and imaging (Figure 1, top).<sup>6</sup> This included pipetting a small amount of the

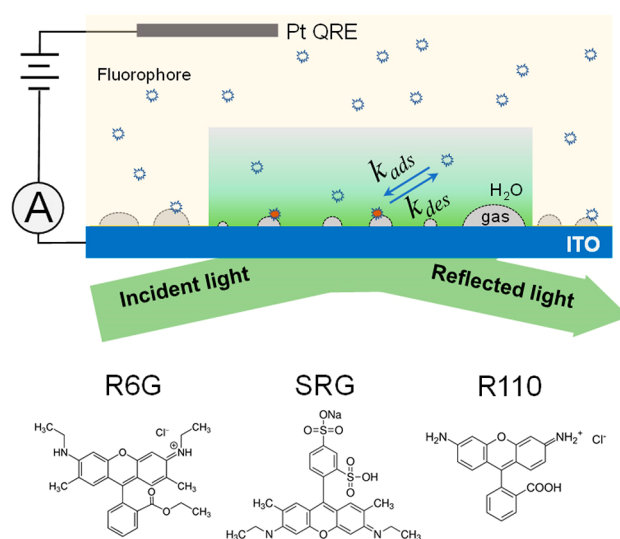


**Figure 1.** (top) Scheme of the experimental setup used for imaging electrochemically generated H<sub>2</sub> nanobubbles. Nanobubbles on the ITO electrodes are dynamically labeled by individual fluorophores and are imaged by TIRF microscopy. (bottom) Molecular structures of the three fluorophores used in this work.

fluorophore solution onto an ITO working electrode that had been thoroughly sonicated in isopropyl alcohol and water, on top of a TIRF objective. A thin sheet of PDMS with millimeter scale holes was used to contain the liquid to a specific area on the working electrode, and a platinum QRE was placed on the top surface of the droplet.

Once a potential is applied across the cell, hydrogen gas is able to be produced from the reduction of water at voltages more negative than −0.75 V vs Pt QRE. Hydrogen gas molecules build up around the surface of the ITO electrode, creating nanosized bubbles, on the surface of which the fluorescent dye molecules subsequently adsorb. The individual dye molecules are excited by the laser and can be detected as a single adsorption event, which can then be counted as a function of fluorophore concentration. As expected, a higher concentration of fluorophore leads to more nanobubble detections, although the number of available nanobubbles is estimated to be fairly comparable at similar applied voltages. Transient fluorophore molecules are unlikely to contribute to the number of detections, due to their fast diffusion through the evanescent field generated by the total internal reflectance setup, shown in Figure S1. Additionally, due to the quenching

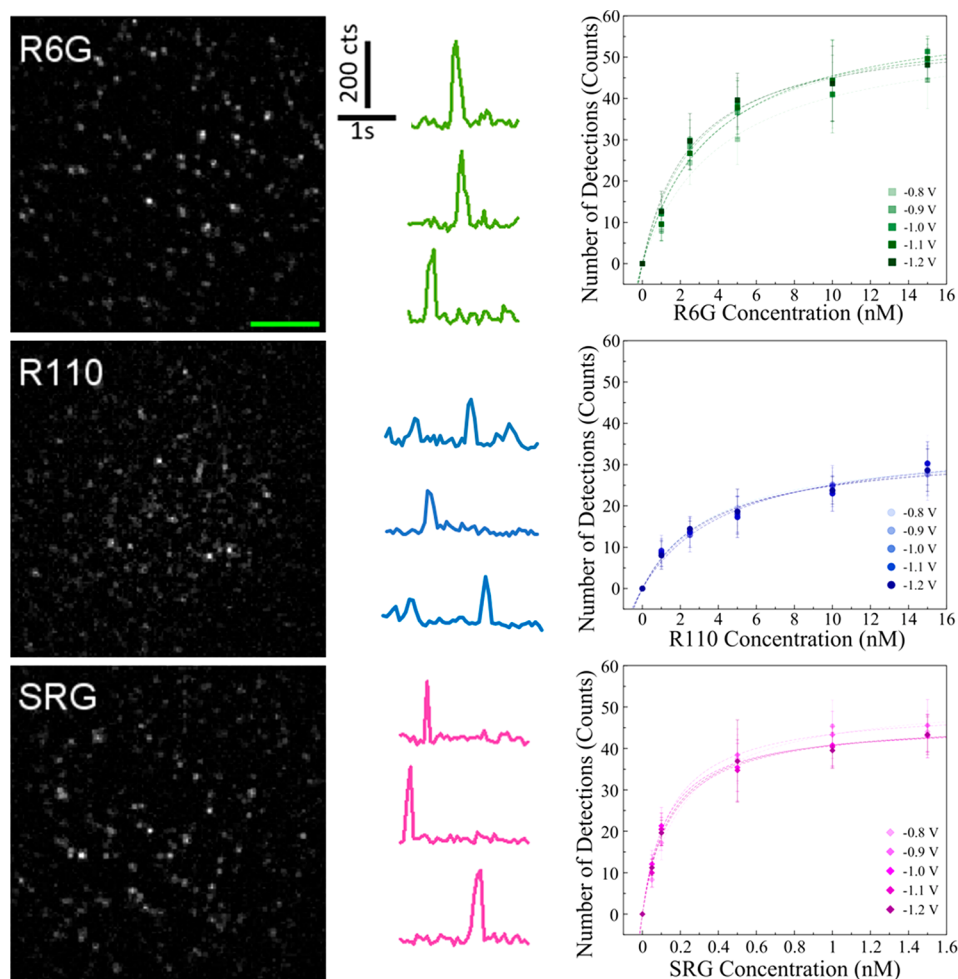


**Figure 2.** Series of TIRF images (left panel) of a  $22.8 \times 22.8 \mu\text{m}^2$  area on an ITO electrode taken from a constant  $-1.0$  V potential vs Pt QRE in water containing  $1$  M  $\text{Na}_2\text{SO}_4$  and  $5$  nM R6G,  $15$  nM R110, or  $0.5$  nM SRG. Fluorescence images were recorded at  $19.81$  frames per second with a  $50$  ms exposure time (Scale bar,  $5 \mu\text{m}$ ). Fluorescence intensity–time traces (middle panel) showing three randomly selected nanobubbles detected at  $-1.0$  V constant potential are shown. Traces were obtained by averaging the total intensity of a  $6 \times 6$  pixel area around a center spot (Scale bar,  $200$  fluorescence counts and  $1$  s) Langmuir adsorption isotherm model fitting (right panel) for R6G, R110, and SRG at five potential conditions. Color from light to dark represents an increase in voltage, step size  $-0.1$  V. Dashed lines represent the Langmuir adsorption fitting curve using eq 2. Error bars in the  $y$ -axis in data points are standard errors from ten repetitive measurements.

ability between the ITO substrate and the fluorophores, it is also unlikely that a detection of the dye would occur without a nanobubble present.

This work strives to understand and quantify the interactions of various fluorophores at the gas/liquid interface, including the equilibrium constant and the residence lifetime of the fluorophore, in addition to the adsorption and desorption rate constants. Three rhodamine-based fluorophores, R6G, SRG, and R110, were used for a comparison study. The three fluorophores have similar excitation and emission wavelength ranges and are structurally alike, each with the same hydrophobic rhodamine core, with varying appendages and functional groups. Both R6G and R110 are positively charged, while SRG is negatively charged. Constant potentials between  $-0.8$  V and  $-1.2$  V were applied to the setup to facilitate the growth of hydrogen nanobubbles. At these potentials the nanobubbles remain relatively stable, allowing for consistent labeling and counting. Figure 2 shows three TIRF images of  $15$  nM R110,  $5$  nM R6G, and  $0.5$  nM SRG with  $1$  M  $\text{Na}_2\text{SO}_4$  at constant  $-1.0$  V vs Pt QRE. These concentrations were chosen to show a consistent number of

detections between the various fluorophores. To monitor the fluorescence intensity of adsorption, multiple fluorescent puncta were randomly selected across several videos, with their intensities measured and plotted over time, three examples of which are shown in the middle panel of Figure 2. The sharp peaks of the intensity traces demonstrate single-molecule adsorption events, followed by a rapid desorption of the fluorophore. The time between adsorption and desorption, where the fluorophore molecule is resting on the surface of the nanobubble, is called the duration, or residence time, and is a subsecond period of near-constant fluorescent intensity.

The application of the Langmuir model is reliant on four assumptions: first, each nanobubble surface is uniform for equivalent adsorption events. Nanobubble generation tends to be stochastic, leading to a variation in their size and shape; however, when a constant potential is applied, the nanobubbles are believed to be dynamically stable. This is due to an equilibrium between gas influx and outflux,<sup>35,36</sup> as well as contact line pinning between the nanobubble and the substrate.<sup>37</sup> The second assumption of the Langmuir model states that there must be no chemical interactions between the

fluorophore molecules and nanobubbles. Rhodamine fluorophores are chemically inert to hydrogen gas, so there is only a physical interaction of adsorption, not a chemical reaction. Third, each adsorption event must be independent. Given the separation between nanobubbles and the dilute concentration of the fluorophore, it is unlikely for one fluorophore adsorption event to influence another on a neighboring nanobubble. Fourth and finally, each nanobubble is considered to be an available site to which only one fluorophore can adsorb. As demonstrated by the intensity measurements in Figure 2 and the results from our previous study,<sup>6</sup> the majority of detections come from single-molecule labeling events. This observation suggests that the fluorophore molecules repel each other when adsorbed on the bubble surface, preventing double- or triple-labeling events from occurring. These experimental conditions allow us to apply the Langmuir model to this gas/liquid interface, which leads to the determination of important equilibrium and kinetic parameters as follows.

To study the single-molecule adsorption/desorption at the bubble surface, it is necessary to derive a more appropriate Langmuir equation to describe our system from the original Langmuir single-site adsorption equation. We use a simple two-step kinetic model of fluorophores at the gas/liquid interface: the freely diffusing fluorophores and trapped fluorophores at the nanobubble surface. The abrupt change in fluorescence intensity can be interpreted as adsorption (increasing intensity) and desorption (decreasing intensity) events, each with a unique rate constant,  $k_a$  and  $k_d$ , respectively. The equilibrium constant,  $K$ , depends on both of these constants and can be written as follows in eq 1:

$$K = \frac{k_a}{k_d} \quad (1)$$

The number of nanobubbles present on the ITO electrode surface can be determined through the amount of fluorophore labeling in a single frame of optical data. Thus, deriving from the original Langmuir equation, we arrive at eq 2, which describes the relationship between the number of detected nanobubbles,  $\gamma^*$ , and the fluorophore's bulk concentration,  $[F]$ .

$$\gamma^* = \frac{\gamma K [F]}{1 + K [F]} \quad (2)$$

where  $K$  is the aforementioned equilibrium constant and  $\gamma$  is the estimated total amount of nanobubbles available on the surface of the ITO electrode at a given voltage condition. It should be noted that the total number of nanobubbles is estimated to be higher than what is visually counted, due to the transient behavior of the fluorophores, as well as the highly dilute dye concentrations used. At low fluorophore concentration,  $[F] \ll K^{-1}$ , eq 2 can be simplified to a linear relationship between the number of detections and the fluorophore concentration:

$$\gamma^* \approx \gamma K [F] \quad (3)$$

Experiments were performed under five different applied potentials:  $-0.8$  V,  $-0.9$  V,  $-1.0$  V,  $-1.1$  V, and  $-1.2$  V. The concentration of each fluorophore was increased to reach the maximum surface coverage, according to the Langmuir model. However, the concentration of the dye cannot be too high because of the increase in fluorescence background and the limited resolution of single-molecule detection. Therefore,

upper and lower limits were determined experimentally, and the resulting range was chosen for study. In Figure 2, equilibrium curves at varying potentials are shown for each of the three dyes, with a best fit line for each condition following eq 2. As can be seen in the figure, there is a more linear trend at lower concentrations of each fluorophore, following the approximation of eq 3. Then, as the concentration increases, the curve gradually levels out and approaches an equilibrium state.

Among these three fluorophores, it is evident that SRG is more effective at labeling nanobubbles, since it is able to reach the same number of detections at much lower concentrations than R6G and R110. This is also demonstrated through the value of  $K$  for each fluorophore, where the equilibrium constant for SRG is an order of magnitude greater than that of the other fluorophores.  $K$  was found through optimizing the best fit parameters, and is shown in Figure 3 for a direct

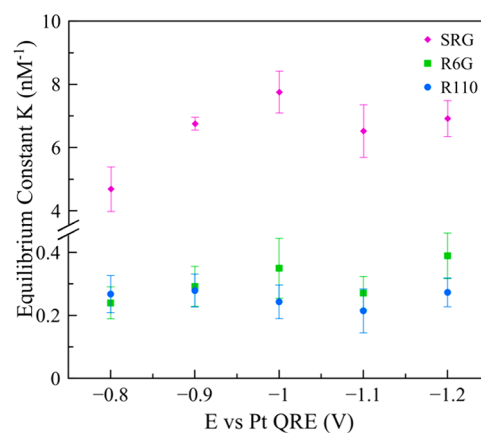
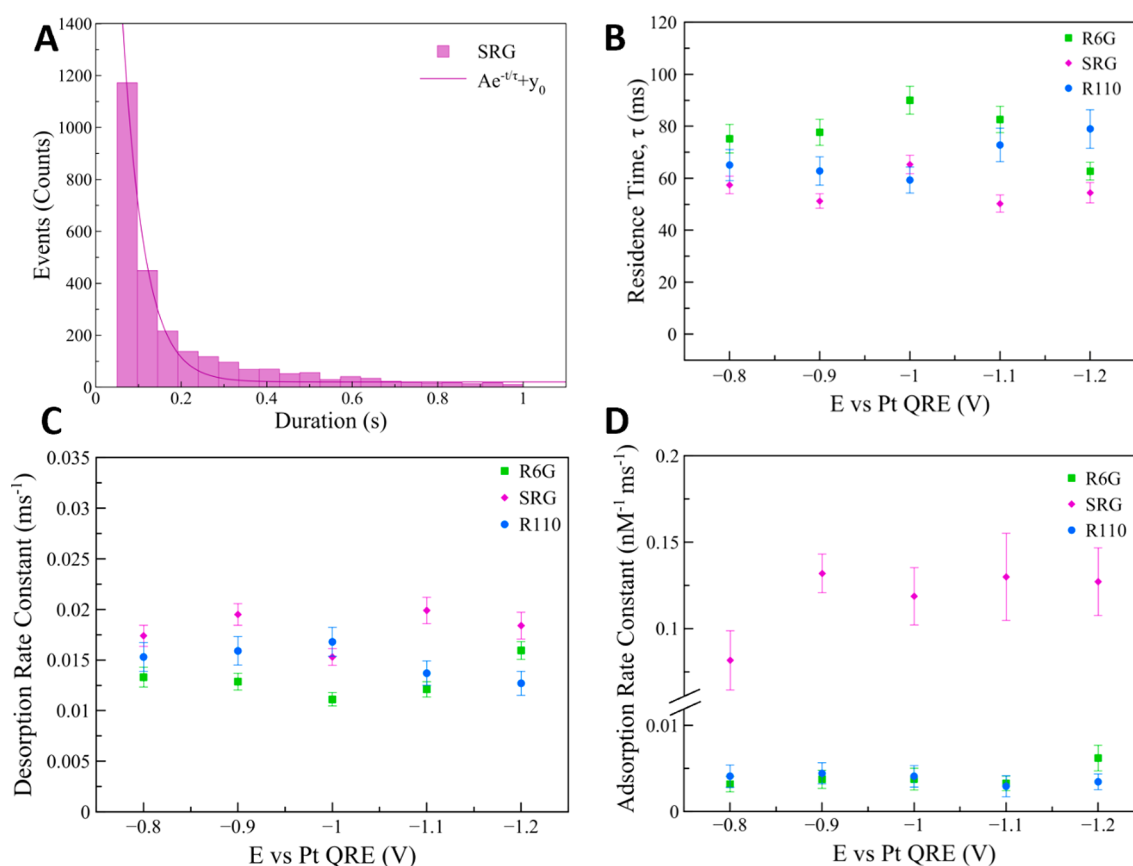


Figure 3. Equilibrium constants for R110, R6G, and SRG at five different applied potentials.

comparison. The discrepancy between  $K$  values can be explained, at least in part, by the charged nature of each species. The structure of SRG (Figure 1B) has a negatively charged sulfonate group attached to a neutral rhodamine core that is hydrophobic in character. The hydrophobic rhodamine core is attracted to the likewise hydrophobic nanobubble surface,<sup>38</sup> leading to increased adsorption and a greater equilibrium constant. This is further supported by the near identical  $K$  values for R6G and R110, both of which have positive charges within the main rhodamine structure, making adsorption less favorable due to having a more hydrophilic nature.

No statistical difference or trend can be determined from the data regarding the various applied potentials. In theory, applying more negative potentials would lead to increased production of hydrogen gas, causing more nanobubbles to be nucleated or existing ones to grow larger. This could change the shape and surface curvature of the nanobubbles, influencing how easily the fluorophores adsorb to the surface and thus affecting the determined equilibrium constant. In this experiment,  $K$  remains more or less constant throughout the varied potentials, which can suggest that either the size and geometry of the nanobubbles do not affect fluorophore labeling or changing the voltage by small increments does not drastically alter said geometry. Evidence supports the latter explanation through the nature of TIRF microscopy. Briefly, the evanescent wave generated by the excitation laser decays



**Figure 4.** Residence time of fluorophores. (A) Example histogram of the duration of nanobubble detection events, taken at  $-0.9$  V vs Pt QRE in  $0.005$  nM SRG with  $1$  M  $\text{Na}_2\text{SO}_4$ . Solid line is the single-exponential decay fit. (B) Scatter plot of fluorophore duration time (ms) under different constant potentials,  $-0.8$  V,  $-0.9$  V,  $-1.0$  V,  $-1.1$  V, and  $-1.2$  V. Rate constants of desorption (C) and adsorption (D) for R6G, R110, and SRG.

exponentially with increasing distance from the ITO electrode surface, which decreases the resulting fluorescence intensity. Thus, having a larger (i.e., taller) nanobubble yields lower intensities. From intensity data collected (Figure S3), there is no significant difference observed across the different voltages, supporting the claim that, at least in this narrow range, the size and geometry of the nanobubbles stays relatively constant.

The equilibrium constant can be further used to gather information about the dynamics of nanobubble labeling. By determining the rate constants for both adsorption and desorption, valuable insights into the interactions between the fluorophore and the nanobubble surface can be made. Using the TrackMate plug-in in ImageJ, the movement and duration of individual spots can be tracked. By plotting the single-molecule duration histogram, the residence time constant of fluorophores can be estimated by fitting with first-order exponential decay, shown in eq 4, and an example is plotted below in Figure 4A.

$$y = A e^{-t/\tau} + y_0 \quad (4)$$

where  $y$  is the number of nanobubbles,  $A$  is the corresponding number of events for time  $t$  with the time constant  $\tau$ , and  $y_0$  is the offset number of nanobubbles. The exponential decay can then be fit to the cumulative residence time histograms, and  $\tau$  is determined.  $\tau$ , or the residence time, is the length of time that a fluorophore is adsorbed on a nanobubble surface and is different from the fluorescence lifetime of the dye. The residence time constants for each fluorophore at each voltage condition are presented in Figure 4B. As with the equilibrium

constant, there is no observed trend from the different potentials, again suggesting that changing the conditions at such increments does not significantly alter the residence time. Averaged across the different voltages, the residence times are as follows:  $74.4 \pm 4.6$  ms,  $55.6 \pm 3.3$  ms, and  $67.0 \pm 5.7$  ms, for R6G, SRG, and R110 respectively. From Figure 4B, it can be seen that SRG has the shortest residence time, perhaps due to the electrostatic interactions at the nanobubble surface. The reduction of water to hydrogen gas produces hydroxide ions, which can build up around the nanobubbles, resulting in a net negative charge at the interface. As mentioned above, SRG has a negatively charged sulfonate group, which could be repelled by excess hydroxide ions as soon as the molecule is adsorbed. The opposite phenomenon, electrostatic attraction, could lengthen the residence time of a positively charged molecule; this is likely the effect on R6G and R110, which both have a positive rhodamine structure. The desorption rate constant,  $k_d$ , can be determined using eq 5:<sup>28</sup>

$$k_d = \frac{1}{\tau} \quad (5)$$

And combined with eq 1, the adsorption rate constant,  $k_a$ , can be determined using eq 6:

$$k_a = k_d K \quad (6)$$

It should be noted that adsorption/desorption rates of fluorophores are derived from the duration time, which could be affected by photobleaching and photoblinking, as these processes also result in the disappearance of a fluorescent spot.

As observed and reported, rhodamine dyes have a much longer lifetime than residence time, which therefore should have negligible effect in determining  $\tau$ .<sup>6</sup> Additionally, a laser is used for constant excitation of the sample, which also lessens the impact of individual fluorophores returning to the ground state and ceasing to fluoresce. The impact of photoblinking can be reduced by bridging neighboring frames with returning fluorescence at the same spot, which could be done with the TrackMate plug-in in ImageJ. Adsorption/desorption rates of R6G, SRG, and R110 at different potentials are calculated and are plotted in Figure 4C,D. Desorption rate constant is the reciprocal of  $\tau$ , so SRG has the greatest  $k_d$ , indicating the fastest desorption of SRG at the bubble surface because of electrostatic repulsion. SRG also has the greatest adsorption rate constant among rhodamine dyes (Figure 4D). This fast rate of adsorption is attributed to the hydrophobic interaction between the neutral, hydrophobic rhodamine core and the hydrophobic bubble surface.

## CONCLUSIONS

In summary, we have used the Langmuir isotherm model to investigate transient adsorption and desorption behavior of single fluorophore molecules at the surface of a nanobubble supported on an ITO electrode. The use of the Langmuir isotherm model allowed us to determine the equilibrium constant and the rate constants for the adsorption and desorption processes. Of the three fluorophores used in this study (R6G, SRG, and R110), SRG was found to have the greatest equilibrium constant, which is likely due to its hydrophobic core. Neither the equilibrium constant nor the rate constants show significant potential dependence within the range of potentials used in this study, which may suggest that the nanobubble size, geometry, and surface properties stay relatively constant within the range of potentials used in this study. Our results suggest that the use of the Langmuir isotherm model is a valid and useful means for probing the unique adsorption behavior of fluorophores at surface-supported nanobubbles. The ability to directly probe and compare the equilibrium constants for different fluorophores (hence how strongly they adsorb at the nanobubble surface) offers a good opportunity for better understanding the chemical nature of the gas/solution interface.

## ASSOCIATED CONTENT

### Supporting Information

The Supporting Information is available free of charge at <https://pubs.acs.org/doi/10.1021/cbmi.3c00020>.

Additional fluorescence TIRF images from the control experiments, additional fluorescence intensity vs time traces for R6G, R110, and SRG, intensity comparisons for R110, R6G, and SRG at various potentials (PDF)

## AUTHOR INFORMATION

### Corresponding Author

Bo Zhang – Department of Chemistry, University of Washington, Seattle, Washington 98195, United States;  
orcid.org/0000-0002-1737-1241; Phone: (1)206 543 1767; Email: zhangb@uw.edu

## Authors

Wes R. Leininger – Department of Chemistry, University of Washington, Seattle, Washington 98195, United States  
Zhuoyu Peng – Department of Chemistry, University of Washington, Seattle, Washington 98195, United States

Complete contact information is available at:  
<https://pubs.acs.org/10.1021/cbmi.3c00020>

## Notes

The authors declare no competing financial interest.

## ACKNOWLEDGMENTS

This research was supported by the National Science Foundation (CHE-2203609).

## REFERENCES

- (1) Heberle, J.; Riesle, J.; Thiedemann, G.; Oesterhelt, D.; Dencher, N. A. Proton Migration along the Membrane Surface and Retarded Surface to Bulk Transfer. *Nature* **1994**, *370*, 379–382.
- (2) Cunliffe, M.; Engel, A.; Frka, S.; Gašparović, B. Ž.; Guitart, C.; Murrell, J. C.; Salter, M.; Stolle, C.; Upstill-Goddard, R.; Wurl, O. Sea Surface Microlayers: A Unified Physicochemical and Biological Perspective of the Air–Ocean Interface. *Prog. Oceanogr.* **2013**, *109*, 104–116.
- (3) Abbatt, J. P. D. Interactions of Atmospheric Trace Gases with Ice Surfaces: Adsorption and Reaction. *Chem. Rev.* **2003**, *103*, 4783–4800.
- (4) Wren, S. N.; Gordon, B. P.; Valley, N. A.; McWilliams, L. E.; Richmond, G. L. Hydration, Orientation, and Conformation of Methylglyoxal at the Air–Water Interface. *J. Phys. Chem. A* **2015**, *119*, 6391–6403.
- (5) Zope, B. N.; Hibbitts, D. D.; Neurock, M.; Davis, R. J. Reactivity of the Gold/Water Interface During Selective Oxidation Catalysis. *Science* **2019**, *330*, 74–78.
- (6) Hao, R.; Fan, Y.; Howard, M. D.; Vaughan, J. C.; Zhang, B. Imaging Nanobubble Nucleation and Hydrogen Spillover during Electrocatalytic Water Splitting. *Proc. Natl. Acad. Sci. U. S. A.* **2018**, *115*, 5878–5883.
- (7) Oja, S. M.; Guerrette, J. P.; David, M. R.; Zhang, B. Fluorescence-Enabled Electrochemical Microscopy with Dihydroresorufin as a Fluorogenic Indicator. *Anal. Chem.* **2014**, *86*, 6040–6048.
- (8) Lu, J.; Fan, Y.; Howard, M. D.; Vaughan, J. C.; Zhang, B. Single-Molecule Electrochemistry on a Porous Silica-Coated Electrode. *J. Am. Chem. Soc.* **2017**, *139*, 2964–2971.
- (9) Suvira, M.; Zhang, B. Effect of Surfactant on Electrochemically Generated Surface Nanobubbles. *Anal. Chem.* **2021**, *93*, 5170–5176.
- (10) James, R. O.; Healy, T. W. Adsorption of Hydrolyzable Metal Ions at the Oxide–Water Interface. III. A Thermodynamic Model of Adsorption. *J. Colloid Interface Sci.* **1972**, *40*, 65–81.
- (11) Zhang, Y.; Cremer, P. S. Interactions between Macromolecules and Ions: The Hofmeister Series. *Curr. Opin. Chem. Biol.* **2006**, *10*, 658–663.
- (12) Knipping, E. M.; Lakin, M. J.; Foster, K. L.; Jungwirth, P.; Tobias, D. J.; Gerber, R. B.; Dabdub, D.; Finlayson-Pitts, B. J. Experiments and Simulations of Ion-Enhanced Interfacial Chemistry on Aqueous NaCl Aerosols. *Science* **2000**, *288*, 301–306.
- (13) Chen, P.; Zhou, X.; Shen, H.; Andoy, N. M.; Choudhary, E.; Han, K. S.; Liu, G.; Meng, W. Single-Molecule Fluorescence Imaging of Nanocatalytic Processes. *Chem. Soc. Rev.* **2010**, *39*, 4560–4570.
- (14) Carrasco, J.; Hodgson, A.; Michaelides, A. A Molecular Perspective of Water at Metal Interfaces. *Nat. Mater.* **2012**, *11*, 667–674.
- (15) Limmer, D. T.; Willard, A. P.; Madden, P.; Chandler, D. Hydration of Metal Surfaces Can Be Dynamically Heterogeneous and Hydrophobic. *Proc. Natl. Acad. Sci. U. S. A.* **2013**, *110*, 4200–4205.

- (16) Orlando, F.; Waldner, A.; Bartels-Rausch, T.; Birrer, M.; Kato, S.; Lee, M. T.; Proff, C.; Huthwelker, T.; Kleibert, A.; Van Bokhoven, J.; Ammann, M. The Environmental Photochemistry of Oxide Surfaces and the Nature of Frozen Salt Solutions: A New in Situ XPS Approach. *Top. Catal.* **2016**, *59*, 591–604.
- (17) Taylor, D. J. F.; Thomas, R. K.; Penfold, J. The Adsorption of Oppositely Charged Polyelectrolyte/Surfactant Mixtures: Neutron Reflection from Dodecyl Trimethylammonium Bromide and Sodium Poly(styrene Sulfonate) at the Air/Water Interface. *Langmuir* **2002**, *18*, 4748–4757.
- (18) Shen, Y. R. Surface Properties Probed by Second-Harmonic and Sum-Frequency Generation. *Nature* **1989**, *337*, 519.
- (19) Hore, D. K.; Beaman, D. K.; Richmond, G. L. Surfactant Headgroup Orientation at the Air/Water Interface. *J. Am. Chem. Soc.* **2005**, *127*, 9356–9357.
- (20) Eisenthal, K. B. Second Harmonic Spectroscopy of Aqueous Nano- and Microparticle Interfaces. *Chem. Rev.* **2006**, *106*, 1462–1477.
- (21) Johnson, C. M.; Baldelli, S. Vibrational Sum Frequency Spectroscopy Studies of the Influence of Solutes and Phospholipids at Vapor/Water Interfaces Relevant to Biological and Environmental Systems. *Chem. Rev.* **2014**, *114*, 8416–8446.
- (22) Bonn, M.; Nagata, Y.; Backus, E. H. G. Molecular Structure and Dynamics of Water at the Water-Air Interface Studied with Surface-Specific Vibrational Spectroscopy. *Angew. Chemie - Int. Ed.* **2015**, *54*, 5560–5576.
- (23) Onorato, R. M.; Otten, D. E.; Saykally, R. J. Adsorption of Thiocyanate Ions to the Dodecanol/Water Interface Characterized by UV Second Harmonic Generation. *Proc. Natl. Acad. Sci. U. S. A.* **2009**, *106*, 15176–15180.
- (24) Otten, D. E.; Shaffer, P. R.; Geissler, P. L.; Saykally, R. J. Elucidating the Mechanism of Selective Ion Adsorption to the Liquid Water Surface. *Proc. Natl. Acad. Sci. U. S. A.* **2012**, *109*, 701–705.
- (25) McCaffrey, D. L.; Nguyen, S. C.; Cox, S. J.; Weller, H.; Alivisatos, A. P.; Geissler, P. L.; Saykally, R. J. Mechanism of Ion Adsorption to Aqueous Interfaces: Graphene/Water vs. Air/Water. *Proc. Natl. Acad. Sci. U. S. A.* **2017**, *114*, 13369–13373.
- (26) Plath, K. L.; Valley, N. A.; Richmond, G. L. Ion-Induced Reorientation and Distribution of Pentanone in the Air-Water Boundary Layer. *J. Phys. Chem. A* **2013**, *117*, 11514–11527.
- (27) Hao, R.; Peng, Z.; Zhang, B. Single-Molecule Fluorescence Microscopy for Probing the Electrochemical Interface. *ACS Omega* **2020**, *5*, 89–97.
- (28) Peterson, E. M.; Manhart, M. W.; Harris, J. M. Single-Molecule Fluorescence Imaging of Interfacial DNA Hybridization Kinetics at Selective Capture Surfaces. *Anal. Chem.* **2016**, *88*, 1345–1354.
- (29) Peterson, E. M.; Reece, E. J.; Li, W.; Harris, J. M. Super-Resolution Imaging of Competitive Unlabeled DNA Hybridization Reveals the Influence of Fluorescent Labels on Duplex Formation and Dissociation Kinetics. *J. Phys. Chem. B* **2019**, *123*, 10746–10756.
- (30) Myers, G. A.; Gacek, D. A.; Peterson, E. M.; Fox, C. B.; Harris, J. M. Microscopic Rates of Peptide–Phospholipid Bilayer Interactions from Single-Molecule Residence Times. *J. Am. Chem. Soc.* **2012**, *134*, 19652–19660.
- (31) Langmuir, I. The Adsorption of Gases on Plane Surfaces of Glass, Mica and Platinum. *J. Am. Chem. Soc.* **1918**, *40*, 1361–1403.
- (32) Swenson, H.; Stadie, N. P. Langmuir's Theory of Adsorption: A Centennial Review. *Langmuir* **2019**, *35*, 5409–5426.
- (33) Ovesný, M.; Křížek, P.; Borkovec, J.; Svindrych, Z.; Hagen, G. M. ThunderSTORM: A Comprehensive ImageJ Plug-in for PALM and STORM Data Analysis and Super-Resolution Imaging. *Bioinformatics* **2014**, *30* (16), 2389–2390.
- (34) Tinevez, J.-Y.; Perry, N.; Schindelin, J.; Hoopes, G. M.; Reynolds, G. D.; Laplantine, E.; Bednarek, S. Y.; Shorte, S. L.; Eliceiri, K. W. TrackMate: An Open and Extensible Platform for Single-Particle Tracking. *Methods* **2017**, *115*, 80–90.
- (35) Weijs, J. H.; Lohse, D. Why Surface Nanobubbles Live for Hours. *Phys. Rev. Lett.* **2013**, *110*, 054501.
- (36) Brenner, M. P.; Lohse, D. Dynamic Equilibrium Mechanism for Surface Nanobubble Stabilization. *Phys. Rev. Lett.* **2008**, *101*, 214505.
- (37) Liu, Y.; Wang, J.; Zhang, X.; Wang, W. Contact Line Pinning and the Relationship between Nanobubbles and Substrates. *J. Chem. Phys.* **2014**, *140*, 054705.
- (38) Peng, Z.; Zhang, B. Nanobubble Labeling and Imaging with a Solvatochromic Fluorophore Nile Red. *Anal. Chem.* **2021**, *93*, 15315–15322.